Eur. Phys. J. A **25**, 211–222 (2005)
DOI 10.1140/epja/i2005-10108-1

THE EUROPEAN PHYSICAL JOURNAL A

# Beta decay of $^{103}$Sn

O. Kavatsyuk[1,2,a], M. Kavatsyuk[1,2], L. Batist[3,4], A. Banu[1], F. Becker[1], A. Blazhev[1,5], W. Brüchle[1], J. Döring[1], T. Faestermann[6], M. Górska[1], H. Grawe[1], Z. Janas[7], A. Jungclaus[8], M. Karny[7], R. Kirchner[1], M. La Commara[4], S. Mandal[1], C. Mazzocchi[1], I. Mukha[1,9], S. Muralithar[1,10], C. Plettner[1], A. Płochocki[7], E. Roeckl[1], M. Romoli[4], M. Schädel[1], R. Schwengner[11], and J. Żylicz[7]

[1] GSI, Darmstadt, Germany
[2] National Taras Shevchenko University of Kyiv, Ukraine
[3] St. Petersburg Nuclear Physics Institute, Russia
[4] Università "Federico II" and INFN, Napoli, Italy
[5] University of Sofia, Bulgaria
[6] Technische Universität München, Germany
[7] University of Warsaw, Poland
[8] Departamento de Fisica Teórica, Universidad Autonoma de Madrid, Spain
[9] Kurchatov Institute, Moscow, Russia
[10] Nuclear Science Center, New Delhi, India
[11] Forschungszentrum Rossendorf, Germany

Received: 3 April 2005 / Revised version: 30 May 2005 /
Published online: 26 August 2005 – 
Communicated by J. Äystö

**Abstract.** The $\beta$ decay of $^{103}$Sn, a three-neutron-particle nucleus with respect to the $^{100}$Sn core, was investigated at the GSI on-line mass separator using an array of 17 germanium crystals and a total absorption spectrometer. A total of 31 $\beta$-delayed $\gamma$-rays (29 new) of the $^{103}\mathrm{Sn} \rightarrow {}^{103}$In decay were observed and, on the basis of $\beta$-$\gamma$-$\gamma$ coincidences, the $^{103}$Sn decay scheme was established for the first time. By means of total absorption spectroscopy, $\beta$ intensities, the Gamow-Teller strength distribution and the summed Gamow-Teller strength value of $3.5 \pm 0.5$ were determined for this decay. Its half-life and $Q_{\mathrm{EC}}$ value were found to be 7.0±0.2 s and 7.64±0.7 MeV, respectively. The $\beta$-delayed proton branching ratio was measured to be $1.2 \pm 0.1\%$. The results are discussed in comparison with shell-model predictions based on realistic and empirical interactions.

**PACS.** 27.60.+j $90 \leq A \leq 149$ – 21.10.-k Properties of nuclei; nuclear energy levels – 23.40.-s $\beta$ decay; double $\beta$ decay; electron and muon capture – 23.20.Lv $\gamma$ transitions and level energies

## 1 Introduction

Since the doubly closed-shell nucleus $^{100}$Sn and some of its neighbouring isotopes were identified [1,2], the study of these very neutron-deficient isotopes has attracted considerable interest. The experimental progress in this field includes in-beam spectroscopy of $^{103}$Sn [3], $^{101}$In [4], $^{99}$Cd [5] and $^{98}$Cd [6,7], the search for direct proton radioactivity in $^{105}$Sb [8,9] and $\beta$-decay studies of $^{101,102}$Sn [10,11], $^{100,102}$In [12,13] and $^{94-98}$Ag [14–18]. Doubly closed-shell nuclei and neighbouring isotopes/-isotones provide a sensitive test ground for the nuclear shell model. $^{100}$Sn is the heaviest doubly-magic $N = Z$ nucleus, located near the proton drip line, where valence protons and neutrons occupy identical shell-model orbitals. As the overlap of their wave functions is large, a strong proton-neutron interaction is expected. The $\beta$ decay of nuclei "southeast" of $^{100}$Sn, *i.e.* with $Z \leq 50$ and $N \geq 50$, is dominated by the Gamow-Teller (GT) transformation $\pi g_{9/2} \rightarrow \nu g_{7/2}$, which in the decay of an even-even nucleus populates the $I^\pi = 1^+$ GT resonance in the daughter nucleus. For an odd-$N$ parent nucleus such as $^{103}$Sn the coupling of this resonance to the unpaired nucleon can be investigated [10,12–14,16–18].

Our intention has been to contribute to studies on the GT $\beta$-decay and on the structure of nuclei near the doubly-magic $^{100}$Sn by investigating the $^{103}$Sn EC/$\beta^+$ decay. Based on shell-model considerations the spins and parities of the $^{103}$Sn and $^{103}$In ground states are likely to be $5/2^+$ [3] and $9/2^+$ [19], respectively. The main part

[a] e-mail: O.Kavatsyuk@gsi.de

of the GT strength is thus associated with the $\beta$ feeding of $3/2^+$, $5/2^+$ and $7/2^+$ levels in $^{103}$In. This disintegration pattern corresponds to dominant feeding of three-quasiparticle states in $^{103}$In, which represent the $\pi(g_{9/2})^{-1}\nu g_{7/2}d_{5/2}$ shell-model configuration spread over many levels. A direct $^{103}$Sn decay to the ground state of $^{103}$In is second-order forbidden and hence very slow. Therefore, one expects that $^{103}$Sn undergoes mainly an allowed proton-to-neutron transformation to high-lying levels of the $\beta$-decay daughter.

The GT strength can be experimentally determined by measuring $\beta$-delayed $\gamma$-rays and particles. The electromagnetic radiation is normally measured by means of high-resolution germanium (Ge) detectors. However, for a case such as $^{103}$Sn it is expected that a significant part of the total $\beta$-decay strength is distributed over many daughter states at high excitation energy, where the level density is very high. Since the $\beta$ feeding to individual levels is often very weak and, moreover, their $\gamma$ de-excitation might proceed through several partly parallel cascades, high-resolution $\gamma$ spectroscopy based on Ge detectors is generally insufficient to determine the complete GT-strength distribution due to the limited detection sensitivity. However, Ge detectors are useful for identifying low-lying levels in the $\beta$-decay daughter. This is the reason why they were employed in this work.

Alternatively, the $\beta$ strength can be obtained from total absorption spectrometry. An advanced total-absorption spectrometer (TAS) was used in this work to study $\beta$ decay of $^{103}$Sn. The TAS consists of a large NaI crystal, a planar Ge detector and a silicon (Si) array for recording $\gamma$-rays, X-rays and charged particles, respectively. The TAS technique is based on recording cascades of $\beta$-delayed $\gamma$-rays, with the energy resolution being poor compared to Ge detectors. The evaluation of TAS data strongly depends on the knowledge of the response function of the TAS for each of the cascades. The information required to obtain the response function concerns excited levels and their de-excitation pattern, which can be determined from high-resolution experiments. Thus, using two complementary methods provides a tool to map the GT-strength distribution, including high excitation energies in the daughter nucleus.

The decay of $^{103}$Sn was studied by using both, the TAS as low-resolution high-efficiency device and an array of Ge crystals including Si detectors for recording positrons (Si-Ge array). In this paper we present the first detailed investigation of the $\beta$-decay properties of $^{103}$Sn, yielding the half-life, the $Q_{\rm EC}$ value, the $\beta$-delayed proton branching ratio, $\beta$-delayed $\gamma$-ray energies and relative intensities, properties of levels in the $^{103}$In daughter nucleus and the summed GT strength value. The experimental techniques are introduced in sect. 2, and the experimental data obtained from the Si-Ge array and TAS are given in sect. 3. A shell-model calculation is discussed in sect. 4, in comparison with experimental results, and sect. 5 presents the summary.

## 2 Experimental techniques

### 2.1 Production and mass separation

The experiment was performed at the GSI on-line mass separator. $^{103}$Sn was produced in the fusion-evaporation reaction $^{50}$Cr($^{58}$Ni, $\alpha$n)$^{103}$Sn. A 4.9 MeV/$u$ $^{58}$Ni beam of about 40 particle-nA from the linear accelerator UNILAC impinged on an enriched $^{50}$Cr target (3 mg/cm$^2$, enrichment 97%). FEBIAD-B2C ion sources with carbon or niobium catchers were used. High chemical selectivity for tin was achieved by adding $CS_2$ vapour to the ion source [20]. Using this technique about 60% of the tin ion-output is shifted to the $SnS^+$ molecular side-band, thus strongly suppressing the isobaric contaminants of indium, cadmium, silver and palladium isotopes. After ionisation, acceleration to 55 keV and mass separation in a magnetic sector field, the ions with $A = 103 + 32$ were directed to the high-resolution array or to the TAS. On the basis of the decay-spectroscopy data, the $^{103}$Sn beam intensity was found to be about 23 atoms/s at a $^{58}$Ni beam intensity of 40 particle-nA.

### 2.2 Si-Ge array

The $A = 103 + 32$ beam from the mass separator was implanted into a tape collector in the center of the Si-Ge array. The implantation point was placed in a vacuum chamber and surrounded by a prism-shaped array of Si detectors (covering 65% of $4\pi$) to record positrons. It consisted of three 1 mm thick individual detectors, with an area of $60 \times 60$ mm$^2$ each and is described in detail in ref. [21]. Around the vacuum chamber an array of 17 individual Ge crystals (including one Euroball Cluster [22] and two GSI VEGA-SuperClover detectors [23]) were placed.

Energy and time events originating from $\beta$-$\gamma$ and $\beta$-$\gamma$-$\gamma$ coincidences between the individual Si and Ge crystals were digitized and written in event-by-event list mode on a magnetic tape. For registering such coincidences, a fast-slow coincidence circuit based on NIM standard electronics was employed. The range of the time-to-digital converters was set to 1 $\mu$s for each individual detector. The accumulation of the data was triggered by a logic "OR" condition of the timing signals originating either from single signals from the individual Ge crystals suppressed by a factor of $2^5$, or from (unsuppressed) $\beta$-$\gamma$ and $\gamma$-$\gamma$ events. The corresponding $\beta$-$\gamma$ coincidence trigger was used to open a time gate of 10 $\mu$s for all amplitude-to-digital converters.

The $\gamma$-ray energies, observed in this work, were calibrated by using known lines from the room background as well as from standard calibration sources such as $^{133}$Ba, $^{152}$Eu and $^{207}$Bi. These sources, placed at the implantation point, were also used to determine the photopeak efficiency as a function of the $\gamma$-ray energy for all Ge counters. It was measured to be 3.2% for 1.33 MeV $\gamma$-ray energy for the single-hit mode, *i.e.*, accumulating the individual events from each Ge crystal. The energy resolution determined as full width at half maximum of the photopeak was about 3 keV at 1.33 MeV $\gamma$-ray energy. The segmentation of the Ge-detector system used

in this experiment was sufficient to keep the summing perturbation of the measured $\gamma$-ray intensities below 10% for a $\gamma$-ray multiplicity of 5 [24].

The main $^{103}$Sn measurement was performed in the grow-in method, *i.e.*, during the time when the $A = 103+32$ beam was continuously implanted into the tape at rest. After a pre-selected time, the tape moved away the buildup activity of $^{103}$Sn decay products from the center of the Si-Ge array. An implantation period of 48 s was chosen in order to optimize the $^{103}$Sn decay rate and to suppress the longer-lived contaminants. The total number of tape cycles amounted to 870, which corresponds to a measuring time of 11.6 h. In addition a measurement (2.1 h) was performed with the $A = 103 + 32$ beam being implanted into the tape for 16 s, followed by a 16 s beam-off period (grow-in/decay method).

### 2.3 TAS

The TAS, which is described in detail in ref. [25], consists of a large NaI crystal with 356 mm length and 356 mm diameter. The pulse-height distribution obtained from this crystal is called "TAS spectrum" in the following. A cylindrical well along the axis of the crystal permits the placement of a source and ancillary detectors in the center of the TAS. The mass-separated $A = 103 + 32$ beam was implanted into a transport tape, with the resulting radioactive sources being regularly moved to the center of the TAS. Here, the implantation point was viewed by two Si detectors (thickness 0.5 mm, diameter 16 mm) situated above (TOP) and below (BOT) the transport tape. Just behind the TOP detector the planar 2 cm$^3$ Ge X-ray (GeX) detector was placed. By demanding coincidence with signals from the Si detectors, the $\beta^+$ component for the decay of interest was selected, whereas coincidences with characteristic $K_{\alpha,\beta}$ X-rays recorded by the GeX detector were used to select the electron capture (EC) mode. The BOT detector, viewing the transport tape from the side of the ion implantation, was used to detect positrons as well as $\beta$-delayed protons.

To deliver fresh radioactive sources and remove the daughter activity, the transport tape was periodically moved. Each implantation-measurement cycle consisted of consecutive periods of 16 and 0.8 s used for implantation and transport, respectively, with the measurement being performed simultaneously with the implantation of the subsequent source. The total number of such cycles was 8090, corresponding to a total measuring time of 36 h.

The TAS spectra obtained with mass-separated activity contain background, in spite of the selectivity of the ion source and the tape cycle. In order to obtain a pure $^{103}$Sn spectrum, the $^{103}$In and $^{103}$Cd contributions to the TAS spectrum have to be determined. For this purpose, we chose implantation-measurement periods of 64 and 800 s and accumulated 630 and 8 such cycles, respectively. To measure the efficiencies of the above-mentioned coincidence gates on characteristic $K_{\alpha,\beta}$ X-rays and positrons, an additional measurement of the $^{106}$Sn decay was performed with 107 cycles of 120 s implantation-measurement time.

**Table 1.** Results obtained from the Si-Ge array measurement: $\gamma$-ray energies ($E_\gamma$), relative $\gamma$-ray intensities ($I_\gamma$) and $\gamma$-$\gamma$ coincidence relationships.

| $E_\gamma$ (keV) | $I_\gamma$(%)[a] | $\gamma$-rays in coincidence (keV) |
|---|---|---|
| 314.0±0.2 | 45±2 | (295), 355, 511, 1356, 1611 |
| 351.3±0.2 | 9±1 | 511, (780), 1078 |
| 355.4±0.2 | 11±1 | 314, 511, (1212), 1356 |
| 627.4±1.4 | 1.2±0.5 | 511, 1397 |
| 635.4±0.5 | 4±1 | 511, 821, 1356 |
| 643.1±0.1[*] | 15±1 | 511 |
| 752.1±0.2 | 8±1 | 511, 1397 |
| 780.0±0.2[*] | 3.0±0.5 | 511, 351 |
| 821.0±0.1 | 12±1 | 511, (635), 1356 |
| 830.6±0.2 | 2.9±0.5 | 511, (1078) |
| 853.0±0.5 | 3.4±0.5 | 511, 1356 |
| 964.3±0.6 | 3±1 | 511, 1356 |
| 993.7±0.3[*] | 7±1 | 511 |
| 1071.3±0.3[*] | 5±1 | 511 |
| 1077.6±0.3 | 22±1 | 351, 511, (831) |
| 1134.5±0.2[*] | 5±1 | 511 |
| 1272.8±0.3 | 1.9±0.5 | 511 |
| 1355.8±0.1 | 100 | 314, 355, 511, 635, 821, (824), 853, 964, (1144), 1611, (1841), 2106 |
| 1396.8±0.1 | 43±2 | 511, 752, 627 |
| 1428.9±0.1[e] | 15±1 | 511 |
| 1548.8±0.3[*] | 4±1 | 511 |
| 1579.8±0.4[*] | 4±1 | 511 |
| 1610.9±0.2 | 13±1 | 314, 511, 1356 |
| 1669.3±0.3[e] | 5±1 | 511 |
| 1840.9±0.4 | 5±1 | 511, 1356 |
| 1908.5±0.5[e] | 4±1 | 511 |
| 1958.8±0.3[*] | 11±1 | 511 |
| 2049.7±0.3[*] | 7±1 | 511 |
| 2106.3±0.3 | 7±1 | 511, (1356) |
| 2209.3±0.3[e] | 4±1 | 511 |
| 2813.2±0.5[e] | 10±2 | 511 |

([a]) Absolute intensities per 100 decays can be derived from the $I_\gamma$ values by multiplying them by a factor of $0.40 \pm 0.05$.
([*]) Transitions tentatively assigned to the $^{103}$Sn decay but not placed in the decay scheme.
([e]) Transitions placed in the level scheme without coincidence relationship but on the basis of known level energies.

## 3 Experimental results

### 3.1 Results of the measurement performed by means of the Si-Ge array

The $\beta$-$\gamma$ and $\beta$-$\gamma$-$\gamma$ coincidence data were sorted off-line into spectra and two-dimensional matrices. The condition for detecting positrons in the Si detectors as full-energy or energy-loss events was set to cover the range of 190 to 2110 keV. The $\gamma$-ray spectrum obtained at mass $A = 103 + 32$ in coincidence with positrons is shown in fig. 1.

The $\gamma$-ray lines at 1078 and 1273 keV were identified by in-beam work [19] to represent transitions in $^{103}$In. In addition to these two transitions, we were able to

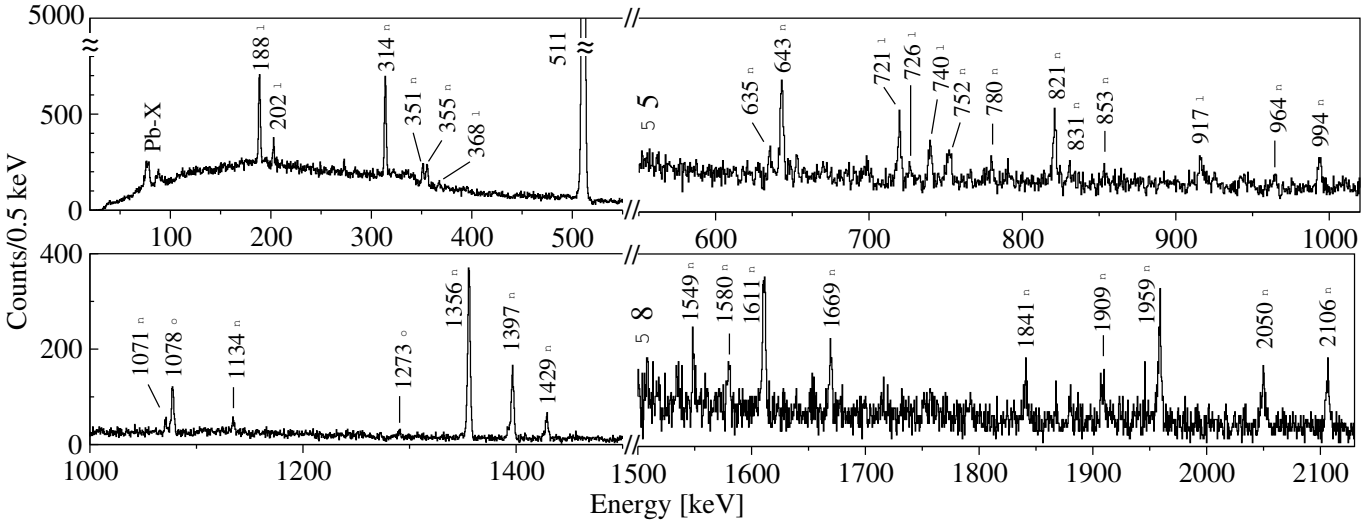


**Fig. 1.** Gamma-ray spectrum obtained for mass 103 + 32 in coincidence with positrons. Gamma rays known to belong to the $^{103}$In decay [26] are marked by circles. The 1078 and 1273 keV lines, marked by open squares, were identified by in-beam spectroscopy [19] as transitions in $^{103}$In. Lines marked by filled squares indicate new $\beta$-delayed $\gamma$-rays which are assigned to the decay of $^{103}$Sn. Energy labels are given in keV. The spectrum in the top panel was scaled by a factor of 5 above an energy of 530 keV and in the bottom panel by a factor of 8 above an energy of 1500 keV.

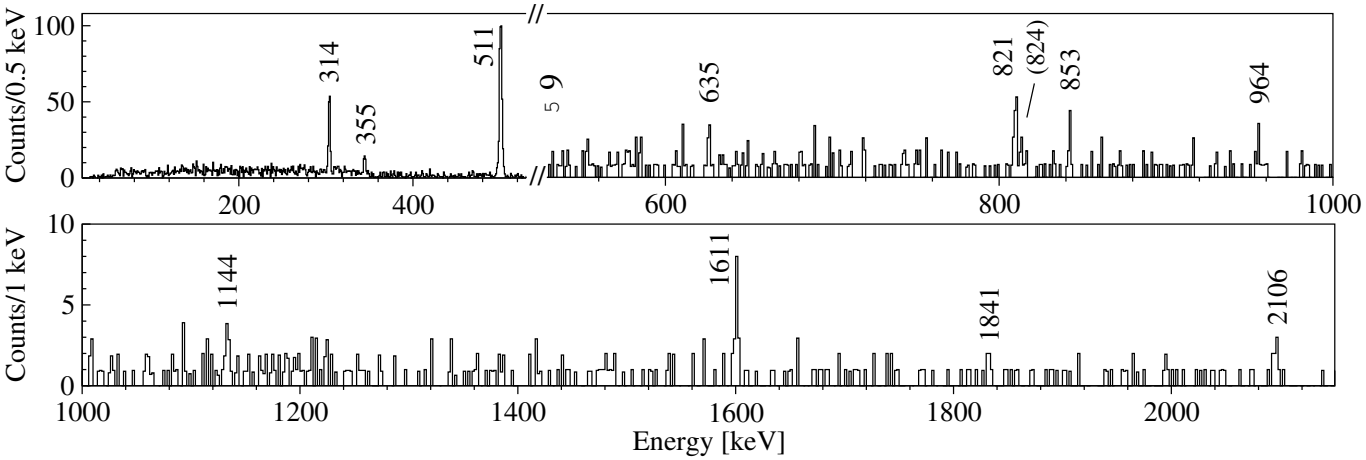


**Fig. 2.** Background-subtracted $\beta$-$\gamma$-$\gamma$ coincidence spectrum, obtained for mass 103+32 with a gate on the most intense 1356 keV line. The spectrum in the top panel was scaled by a factor of 9 above an energy of 530 keV.

unambiguously assign 20 new $\gamma$ lines to the $^{103}$Sn decay. Gamma rays in $^{102}$Cd such as the 777 keV $2^+ \rightarrow 0^+$ transition, that may be emitted after $\beta$-delayed proton decay of $^{103}$Sn, were not observed in the spectrum displayed in fig. 1. This is due to the fact that this disintegration mode has a small branching ratio and is mainly connected with EC decay, as will be discussed in sect. 3.2.3

The results obtained from this measurement are summarised in table 1. The relative $\gamma$-ray intensities were obtained from the $\beta$-gated $\gamma$-ray spectrum. For this purpose, the original intensities were corrected for the energy-dependent efficiency of the Ge detectors and normalised to the intensity of the 1356 keV line, neglecting summing corrections.

The assignment of the 314, 1356 and 1397 keV $\gamma$-rays to the $^{103}$Sn decay was based on experimental half-lives.

**Table 2.** Half-life of $^{103}$Sn determined by using the Si-Ge array and the TAS (see text). The weighted average half-life is calculated from the six individual values.

| Spectrum condition | $T_{1/2}$ (s) |
|---|---|
| $\gamma$-rays 314 (grow-in) | $7.2 \pm 0.7$ |
| $\gamma$-rays 314 (grow-in/decay) | $7.8 \pm 0.9$ |
| $\gamma$-rays 1356 (grow-in) | $6.7 \pm 0.6$ |
| $\gamma$-rays 1356 (grow-in/decay) | $6.6 \pm 0.8$ |
| $\gamma$-rays 1397 (grow-in) | $7 \pm 1$ |
| Protons with energies above $E_p \geq 3$ MeV | $7.0 \pm 0.5$ |
| Protons in anticoincidence with TAS | $7.0 \pm 0.4$ |
| | $\overline{T_{1/2}} = 7.0 \pm 0.2$ |

Table 2 shows results of fits to measured time profiles using the maximum-likelihood method. They stem from

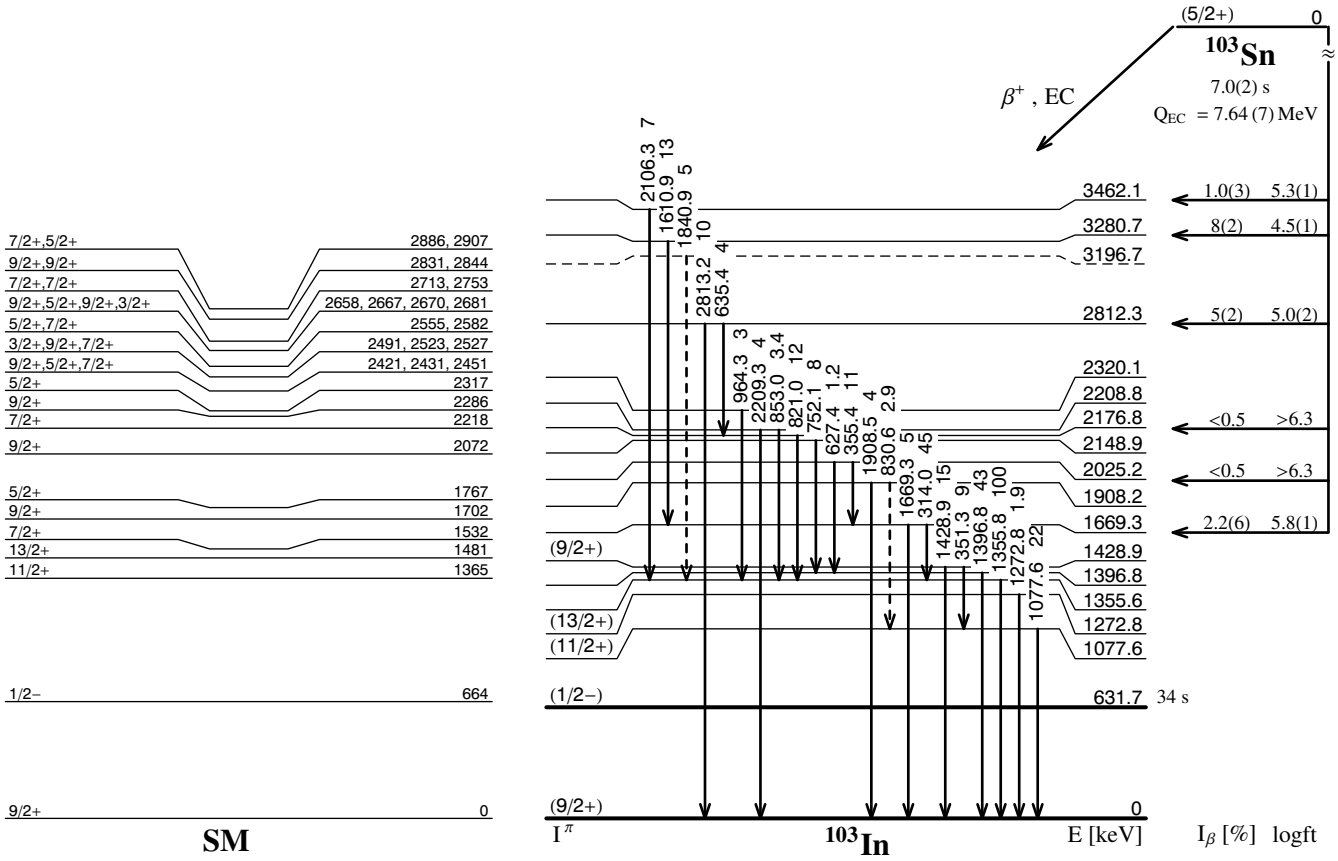


**Fig. 3.** Proposed scheme of $^{103}$In levels fed in the decay of $^{103}$Sn compared with shell-model calculations [30,31] (Model A, see sect. 4.2). Transitions in $^{103}$In are marked by their energies in keV and relative intensities in %. Spin and parity assignments were taken from [19] (except for 1429 keV level). Transitions and levels marked by dashed lines are placed tentatively in the decay scheme. The $\beta$ intensities ($I_\beta$ in %) and $\log ft$ values represent TAS results. For the shell-model predictions, all $3/2^+$, $5/2^+$, $7/2^+$ and $9/2^+$, but only the first $1/2^-$, $11/2^+$ and $13/2^+$ $^{103}$In levels are shown.

$\beta$-delayed $\gamma$-ray (48 s grow-in and 16 s/16 s grow-in/decay) or proton data (see sect. 3.2.3). The lower accuracy of the half-life values deduced from the measurement in grow-in/decay mode is due to the short measurement time, *i.e.* poor statistics. The weighted average of the $^{103}$Sn half-life is 7.0±0.2 s. This result is in agreement, but considerably more accurate than the previously obtained values of $7 \pm 3$ s [27] and $7.5 \pm 1.5$ s [28]. It deviates, however, from the result of $8.7 \pm 0.6$ s [29].

Further information for constructing the $^{103}\mathrm{Sn} \rightarrow {}^{103}\mathrm{In}$ decay level-scheme stems from the $\beta$-$\gamma$-$\gamma$ coincidence data which are included in table 1. As an example, the background-corrected $\gamma$-ray spectrum obtained in coincidence with 1356 keV line is shown in fig. 2. The resulting decay scheme, displayed in fig. 3, includes 23 of the 31 $\gamma$ transitions that were assigned to represent $\beta$-delayed $\gamma$-rays of $^{103}$Sn. The 1078 and 1273 keV $\gamma$-rays are known to represent transitions from the $(11/2^+)$ to the ground state and from the $(13/2^+)$ to the ground state [19]. The cascades feeding levels at 1078, 1356 and 1397 keV were established by using $\gamma$-$\gamma$ coincidence relationships. The 1429 keV level, based on the coincidence relationship between the 1078 and 351 keV transitions, is supported by the observation of the 1429 keV transition which is interpreted as a cross-over transition from this level to the ground state. This 1429 keV transition competes with the 351 keV one, for which the $E2$ multipolarity is likely excluded. Therefore, the 1429 keV level is most probably a $9/2^+$ state, as the transition from the $^{103}$Sn ground state $(5/2^+)$ to the $11/2^+$ state in $^{103}$In is forbidden, and an $E2$ would be required for the $(7/2^+) \rightarrow 11/2^+$ one. In a similar way like for 1429 keV line the 1669 keV transition supporting a level established by the 1356 and 314 keV lines was placed, as well as the 2209 keV ($2209 = 853 + 1356$), 2813 keV ($2813 \approx 1356 + 821 + 635$) and 1909 keV ($1909 = 1078 + 831$) transitions. These four lines were considered to represent cross-over $\gamma$ transitions, with only minor contribution due to summing effect (see sect. 2.2). The nine lines marked by asterisks in table 1 have been observed in coincidence with the 511 keV annihilation peak only (except for 780 keV line). In view of this fact and the low statistics of these lines which make a half-life determination unreliable, it was considered unsafe to include these lines into the decay scheme of $^{103}$Sn. The possible placement of the 643 keV transition is discussed in sect. 3.3. The apparent $\beta$ intensities and $\log ft$ values, deduced from such a (partial) level scheme, are unreliable due to the problem of missing (weak) $\gamma$-rays in high-resolution

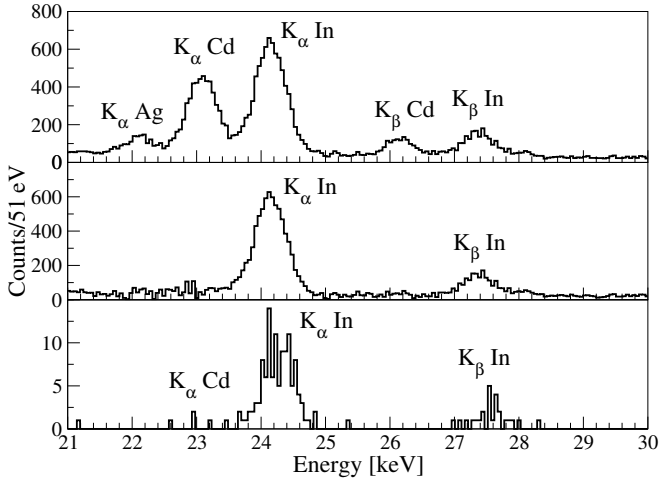


**Fig. 4.** X-ray spectra registered during the $A = 103 + 32$ measurement by the GeX detector before (upper panel) and after (middle panel) subtraction of contributions from contaminants, and in coincidence with protons registered in the BOT detector (lower panel). Peaks assigned to the decay of $^{103}$Sn, $^{103}$In, $^{103}$Cd, corresponding to the observation of In, Cd and Ag X-rays, respectively, are accordingly labelled.

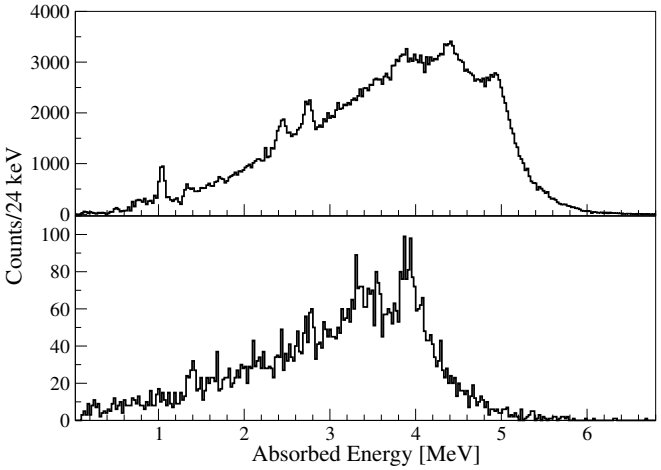


**Fig. 5.** Upper panel: TAS spectrum gated by the TOP and BOT detectors, selecting the $\beta^+$ component of the $^{103}$Sn decay. The $^{103}$In and $^{103}$Cd contamination has been subtracted. Lower panel: TAS spectrum representing the EC component of the $^{103}$Sn decay. The latter data were obtained by gating on In $K_\alpha$ X-rays measured by the GeX detector.

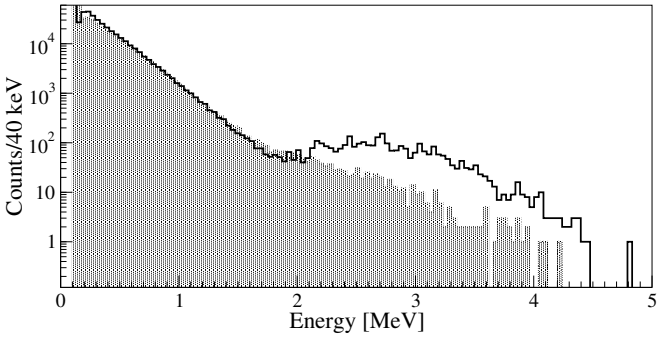


**Fig. 6.** Spectrum of $\beta$-particles and protons from the $^{103}$Sn decay, measured by the BOT (black-line histogram) and TOP (shaded-area histogram) detectors.

studies. The $\beta$ intensities and log $ft$ values shown in fig. 3 were obtained from the TAS data (see sect. 3.2.2).

## 3.2 Results of the TAS measurement

### 3.2.1 Experimental TAS spectra

As the singles TAS spectrum is dominated by contributions from the room background, $^{103}$Sn decay events were selected by using the ancillary detectors. The GeX detector was employed to measure the characteristic X-rays emitted after EC processes. The resulting X-ray spectrum is shown in the upper panel of fig. 4. The peaks of In, Cd and Ag X-rays can be assigned to the EC decay of $^{103}$Sn, $^{103}$In and $^{103}$Cd, respectively, provided the contributions of conversion electrons from transitions in the respective daughter nuclei can be neglected. By demanding coincidence between the TAS signal and the characteristic In X-ray measured by the GeX detector, the EC component of the $^{103}$Sn decay was selected. The resulting TAS spectrum (TAS(EC)) is shown in the lower panel of fig. 5. The absorbed-energy scale of this figure and all following TAS spectra is only approximate as the correspondence between peak position in the TAS spectra and $^{103}$In level energies depends on the de-excitation path, see ref. [32] for details. The TAS(EC) spectrum does not suffer from the isobaric contaminant because of the high resolution of the GeX detector.

The TOP and BOT detectors were used to register positrons and protons (see fig. 6). The exponential low-energy events are assigned to positrons while the "bump" above about 2 MeV is interpreted as being due to $\beta$-delayed protons (see sect. 3.2.3). The latter events registered by the TOP detector are shifted to lower energies due to the energy loss of protons in the tape. The energy range between 0.2 and 1.8 MeV was used as a positron condition for both Si detectors. Events observed in the BOT detector, which have energy deposits larger than 2.5 MeV were considered to stem from protons. By demanding coincidence of the TAS signal with signals from the TOP or/and BOT detector within the positron gate, the $\beta^+$ component of the decay was obtained (TAS($\beta^+$)). On the basis of the additional measurements with longer tape cycles (see sect. 2.3), the $^{103}$In and $^{103}$Cd contributions were subtracted from the total TAS($\beta^+$) spectrum obtained for $A = 103{+}32$. The subtraction coefficients were determined by using the X-ray spectra for normalisation. For this purpose, the GeX spectra obtained from the long-cycle measurements (see sect. 2.3) were subtracted from the GeX spectrum of the main measurement until the peaks of characteristic Ag and Cd X-rays disappeared. The resulting GeX spectrum is shown in the central panel of fig. 4, while the corresponding background-free TAS($\beta^+$) spectrum is displayed in the upper panel of fig. 5. All in all, it was

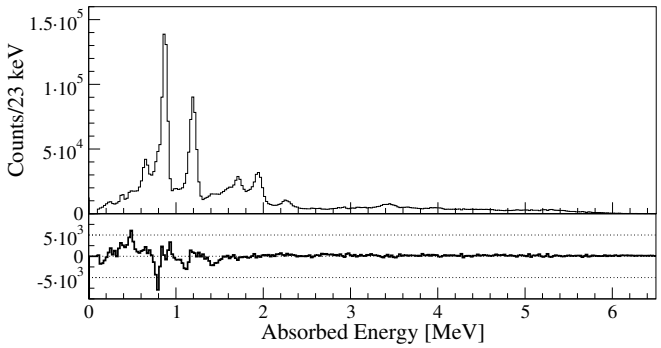


**Fig. 7.** Upper panel: Background-free singles TAS spectrum of the $^{106}$Sn decay (thick-line histogram) and sum of the TAS(EC) and TAS($\beta^+$) spectra divided by corresponding gate efficiencies (grey-line histogram). Lower panel: Difference between the spectra displayed in the upper panel.

found that the total TAS($\beta^+$) spectrum contained a fraction of 23% due to contributions of isobaric contaminants.

The efficiency of the gate conditions set on the Si and GeX signals was deduced from the $^{106}$Sn data (see sect. 2.3). In this case the singles TAS spectrum was used, after subtracting the contribution from the room background determined in a separate measurement. The resulting TAS spectrum is shown in the upper panel of fig. 7. The singles background-free TAS spectrum consists of $\beta^+$ and EC contributions from the decay of interest and from contaminants. In the first-order approximation the Si gated TAS spectrum contains only the $\beta^+$ component but with reduced statistics compared to the singles TAS spectrum. The reduction factor represents the efficiency of the corresponding gate ($\varepsilon_{\rm Si}$). The same assumption can be used for conditions on In and Cd X-rays measured by the GeX detector ($\varepsilon_{\rm GeX,In}$, $\varepsilon_{\rm GeX,Cd}$). However, this approach works only for events where all prompt $\gamma$-rays are absorbed by the TAS. Otherwise, there is the probability of registering $\gamma$-rays in the GeX or Si detectors, which depends on the $\gamma$-de-excitation pattern in the daughter nucleus. The condition of 100% total-absorption efficiency is fulfilled only for the photopeaks. Therefore, during the decomposition of the singles TAS spectrum only photopeaks were taken into account. The resulting sum of the TAS(EC) and TAS($\beta^+$) spectra, corrected for gate efficiencies of $\varepsilon_{\rm Si} = 88 \pm 1\%$ and $\varepsilon_{\rm GeX,In} = 6.6 \pm 0.5\%$, respectively, is shown in the upper panel of fig. 7. During the decomposition, only the $^{106}$Sn and $^{106}$In EC-decay components were taken into account. The small disagreement between the two spectra, displayed in the lower panel of fig. 7, is due to neglecting the $^{106}$Cd EC-decay component.

The total number of counts in the TAS(EC) and TAS($\beta^+$) spectra measured for the $^{103}$Sn decay as well as the efficiencies of the gate conditions were used to determine the EC/total ratio. However, to take into account the probability of registering $\gamma$-rays in the GeX detector, a small correction of $0.92 \pm 0.02$ was applied to the $\varepsilon_{\rm GeX,In}$ value. This correction factor was deduced from a Monte Carlo simulation of the $^{103}$Sn decay. The resulting EC/total value was found to be $0.20 \pm 0.02$.

### 3.2.2 Beta-intensity distribution

In order to determine the $\beta$-intensity distribution for $^{103}$Sn, a set of TAS spectra corresponding to the population of selected $^{103}$In levels was simulated and fitted to the experimental TAS spectra by a least-squares method, with the $\beta$ intensities of these levels being variable parameters.

The simulations were performed by using the Monte Carlo code GEANT-4 [33]. To perform the simulation for a TAS spectrum corresponding to the population of a selected $^{103}$In level the knowledge of its de-excitation pattern is required. Therefore the level scheme obtained from the high-resolution measurement (see sect. 3.1) was used as an input for the simulation. However, the low efficiency of the high-resolution setup means that weak $\beta$-delayed $\gamma$ transitions have remained unobserved. Correspondingly, the decay scheme shown in fig. 3 is incomplete, and hence assumptions have to be made in deducing $\beta$ intensities. To overcome this problem, additional $^{103}$In levels were introduced. For this purpose, a shell model calculation [30, 31] (see also sect. 4.2, *Model A*) of $^{103}$In excited levels in the spin range between 1/2 and 21/2 was performed, yielding 4900 levels within the $Q_{\rm EC}$ value of 7.64 MeV (see below). Among them 800 levels have $3/2^+$, $5/2^+$ or $7/2^+$ spin-parity, thus were assumed to be populated in the $^{103}$Sn $\beta$-decay. However, each of these level adds additional parameters to the deconvolution procedure. In order to reduce the number of fit parameters, the range of $^{103}$In excitation energies above 2.5 MeV was divided into 90 energy intervals ($\Delta E_i$) of 50 keV width which were treated as "single levels" populated in $\beta$ decay.

To simulate a $\beta$-decay event a sequence of subevents, namely X-ray or positron emission followed by prompt $\gamma$-rays, was generated as an input to the detector-simulation programme. The generation of the prompt $\gamma$ cascade depends on the type of the initial level. In case of a $\beta$ decay to one of the levels known from the high-resolution measurement ($L_j$) the de-excitation pattern was taken from the scheme shown in fig. 3. However, to simulate the response function of the TAS for a $\beta$ decay to the interval $\Delta E_i$ additional assumptions had to be made. The spin-parity $I^\pi$ of the initial energy interval was drew for each simulated event to be $3/2^+$, $5/2^+$ or $7/2^+$. Further de-excitation of the levels within $\Delta E_i$ is possible via a $\gamma$ transition to another energy interval or to one of the experimentally established levels $L_j$. The probability of the $\Delta E_i(I_i^\pi) \rightarrow \Delta E_f(I_f^\pi)$ transition was assumed to be $b_{\Delta E}(i, I_i^\pi | f, I_f^\pi) = \sum_{k \in M_f, \chi} F_\chi(\overline{E_i}, I_i^\pi; E_f^k, I_k^\pi)$, where $F_\chi(E_1, I_1^\pi; E_2, I_2^\pi)$ is the probability of the electromagnetic transition of the type $\chi \in \{E1, E2, M1\}$ between the excitation energies $E_1$ and $E_2$ determined by statistical models ($E1$ [34], $M1$ [35], $E2$ [36,37]). The ensemble $M_f$ consists of the levels predicted by the shell model calculation to lie within the energy interval $\Delta E_f$. In case of transitions from the energy interval $\Delta E_i$ to one of the known levels $L_f$ the probability was calculated as $b_L(i, I_i^\pi | f, I_f^\pi) = C_f \sum_\chi F_\chi(\overline{E_i}, I_i^\pi;\, E_f, I_f^\pi)$, where $C_f$ are coefficients introduced in order to reproduce the relative $\gamma$-ray intensities listed in table 1.

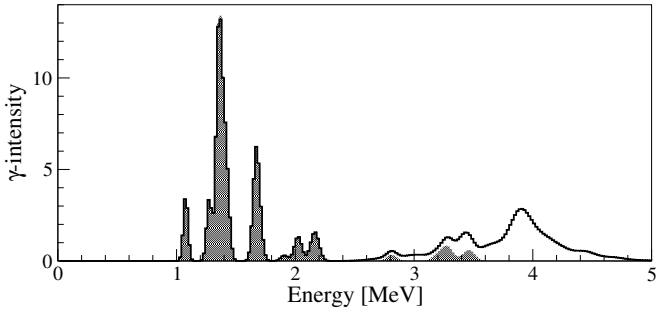


**Fig. 8.** Intensities of the $\beta$-delayed $\gamma$-rays from the $^{103}$Sn decay as a function of the $^{103}$In excitation energy. The $\gamma$ intensity is defined as the number of quanta emitted per 100 decays, integrated over an excitation energy interval of 20 keV. The TAS results (black-line histogram) are compared to data obtained by the Si-Ge array (shaded-area histogram). The latter distribution has being folded with the TAS resolution.

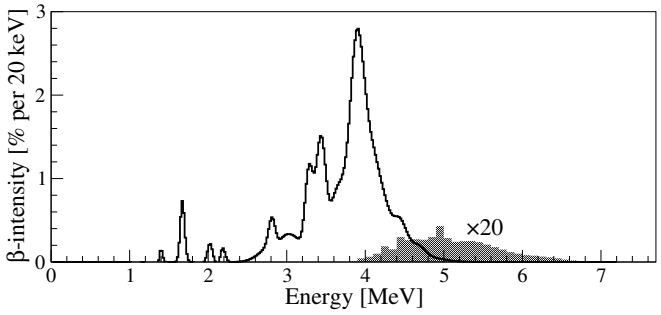


**Fig. 9.** Beta-intensity distribution for the $^{103}$Sn decay obtained by measuring $\beta$-delayed $\gamma$-rays (black-line histogram) and $\beta$-delayed proton emission (shaded-area histogram).

In order to verify the above-mentioned assumptions, an additional criterion is needed. Once the $\beta$ intensities ($I_\beta$) are determined from the fit procedure it is possible to deduce the $\gamma$-intensity ($I_\gamma$) spectrum which shows how many $\gamma$ quanta depopulate a certain $^{103}$In level. In case of the correct construction of the level scheme including the energy intervals, and the correct determination of the $I_\beta$ distribution, the $\gamma$ intensities deduced for the experimentally known levels $L_i$ should be the same as those determined from the high-resolution measurement. When the level scheme used for the simulation is wrong, the corresponding $I_\gamma$ spectra obtained from the fit and experiment will disagree. To correct such a discrepancy the above-mentioned coefficients $C_f$ were changed. After matching the $C_f$ values a new simulation was performed to determine the TAS response functions, and the fitting procedure was repeated. Such iterations were made until agreement between experimental and simulated $I_\gamma$ spectra was reached. The corresponding $I_\gamma$ spectra are shown in fig. 8. Below 2.5 MeV, the two curves agree. However, above 2.5 MeV the TAS measurement shows higher $\gamma$ intensities because in this excitation energy region close-lying and weakly-populated $^{103}$In levels exist, whose identification is impossible with the Ge array used in this work.

During the deconvolution procedure the TAS($\beta^+$) and TAS(EC) spectra were fitted simultaneously with the $^{103}$Sn $Q_{\mathrm{EC}}$ value being a fixed parameter. The resulting $I_\beta$ distribution allowed us to determine the EC/total ratio, which strongly depends on the $Q_{\mathrm{EC}}$ value assumed during the fit. By repeating the fitting procedure for different $Q_{\mathrm{EC}}$ values the experimental EC/total value of $0.20 \pm 0.02$ mentioned in sect. 3.2.1 was reproduced, the corresponding $Q_{\mathrm{EC}}$ value for the $^{103}$Sn decay being $7660 \pm 100$ keV.

The final $I_\beta$ distribution is shown in fig. 9. The TAS data give evidence for the population of the 1670, 2025, 2177, 2812, 3281 and 3462 keV levels obtained from the high-resolution measurement. For the other levels, shown in fig. 3, the TAS measurement excludes $\beta$ intensities above a level of about 0.5%.

The TAS data for the $^{103}$Sn decay show no direct $\beta$ feeding of the $^{103}$In ground state. The 1022 keV peak in the TAS($\beta^+$) spectrum, displayed in fig. 5, corresponds to an escape of a $\gamma$-ray depopulating a $^{103}$In level by a single $\gamma$ transition. A simple estimate based on the assumption that all counts in the 1022 keV peak correspond to the direct ground-state feeding gives an upper limit of 1% for the $\beta$ intensity of the ground-state–to–ground-state decay. This result will be further discussed in sect. 4.3.

### 3.2.3 Beta-delayed proton properties

Beta-delayed protons of the $^{103}$Sn decay were registered by the BOT detector. However, the thin layer of air (0.65 mm) between the source and BOT detector did not allow us to make an accurate energy calibration. A $^{148}$Gd $\alpha$-source was used as a high-energy calibration point of 3.18 MeV. In order to take into account the energy losses of $\alpha$-particles in air, the corresponding response of the BOT detector was simulated by the Monte Carlo toolkit GEANT-4 [33] and compared with the measured spectrum. The 662 keV conversion-electron peak, observed by using a $^{137}$Cs source, was used as an additional calibration point. The resulting accuracy of the energy calibration for protons was about 100 keV.

The TAS enables one to identify the final states populated in $\beta$p decay by detecting $\gamma$-rays following proton emission. Moreover, the total absorption effect in the TAS allows one to discriminate between the EC and $\beta^+$ decay modes. The TAS spectrum measured in coincidence with protons emitted in the $\beta$ decay of $^{103}$Sn is shown in fig. 10. The 777 keV peak corresponds to the $\beta$p decay to the first excited state in $^{102}$Cd after EC (ECp) decay. The 1022 keV peak stems from proton transitions to the $^{102}$Cd ground state after positron ($\beta^+$p) decay of $^{103}$Sn. The trace of the $777+1022$ keV peak in fig. 10 indicates the $\beta^+$p feeding of the 777 keV state in $^{102}$Cd. The energy shift of 1022 keV between the ECp and $\beta^+$p peaks is due to the absorption of two 511 keV quanta, whereas the ECp decay to the ground state of the $^{102}$Cd is characterised by the absence of TAS signals. The $\beta$p-gated TAS spectrum was decomposed into four contributions from $\beta^+$p and ECp transitions to ground and first excited states of $^{102}$Cd by

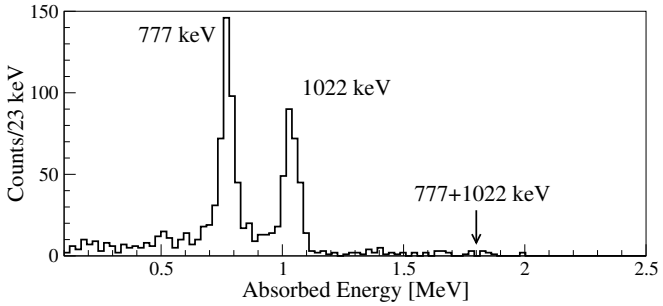


**Fig. 10.** TAS spectrum gated by $\beta$-delayed protons from the $^{103}$Sn decay.

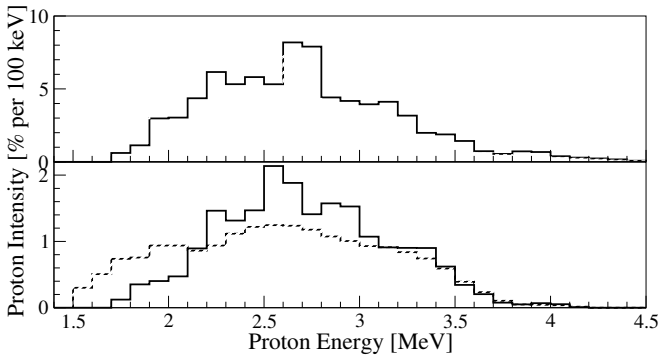


**Fig. 11.** Intensities of the $\beta$-delayed proton decay of $^{103}$Sn, obtained in the experiment (solid-line histograms) and from statistical model calculations (dashed-line histograms). Upper panel: proton intensities for the $^{103}$Sn $\beta$p decay to the $^{102}$Cd ground state. Lower panel: proton intensities for $\beta$p decay to the $2^+$ level in the $^{102}$Cd.

using the simulated TAS response functions. However, the branching ratios obtained for these states are related to the *entire* proton spectrum of the $^{103}$Sn decay within the proton window and, therefore, should be corrected by using the proton spectra of each decay component.

The proton spectrum of the ECp decay to the ground state of $^{102}$Cd was obtained by demanding anticoincidences of the BOT signals with those from TAS. However, the low-energy part of the resulting spectrum contains a contribution from conversion electrons emitted in the decay of the 632 keV $1/2^-$ isomer of $^{103}$In, which will be discussed in sect. 3.3. The protons corresponding to the $\beta^+$p mode feeding the ground state and the ECp component feeding the $2^+$, 777 keV state of $^{102}$Cd were selected by gating on the 1022 keV and 777 keV lines in the TAS spectrum, respectively. To avoid summation of the proton and positron signals, the $\beta^+$p spectrum was additionally gated by $\beta$-particles registered in the TOP detector. The proton spectra for all above-mentioned components contain some positron contribution in their low-energy part. Nevertheless the $\beta$p events are generally well separated from positrons and conversion electrons. The only exception is the proton spectrum of the $\beta^+$p component feeding the $2^+$, 777 keV state in $^{102}$Cd, which was obtained by setting a 1.3 to 1.8 MeV gate in the TAS spectrum (777 + 1022 keV line with corresponding Compton tail)

**Table 3.** Experimentally determined relative branching ratios for $\beta$-delayed proton decay of $^{103}$Sn to $^{102}$Cd states of excitation energy $E_f$ and spin-parity $I^\pi$.

| $E_f$ (keV) | $I^\pi$ | Decay mode | $\beta$p branching ratio (%) |
|---|---|---|---|
| 0 | $0^+$ | ECp | $46 \pm 2$ |
| 0 | $0^+$ | $\beta^+$p | $20 \pm 1$ |
| 777 | $2^+$ | ECp | $32 \pm 2$ |
| 777 | $2^+$ | $\beta^+$p | $\leq 2$ |

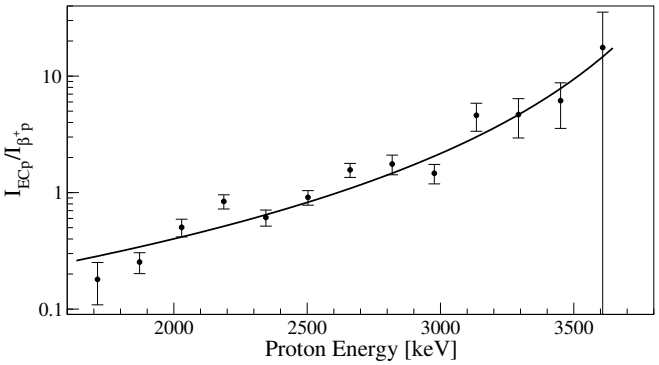


**Fig. 12.** $I_{\mathrm{ECp}}/I_{\beta^+\mathrm{p}}$ ratio as a function of proton energy for the $^{103}$Sn $\beta$p-decay to the ground state of $^{102}$Cd. The solid line represents the best fit of the theoretical $I_{\mathrm{ECp}}/I_{\beta^+\mathrm{p}}$ data to the experimental results, yielding a $Q_{\mathrm{EC}} - S_{\mathrm{p}}$ value of $5400 \pm 100$ keV.

and requiring positrons to be registered in the TOP detector. In this case, the low statistics and the positron background did not allow us to unambiguously identify $\beta$p events. This component has, however, a small branching ratio (less than 2%) and is thus neglected in the further analysis. All proton spectra were normalised by using branching ratios obtained from the decomposition of the $\beta$p-gated TAS spectrum. The efficiency for registering protons in the BOT detector was determined by Monte Carlo simulations. The resulting response functions of the BOT detector for 1.5 to 5 MeV protons were used for deconvoluting the experimental proton spectra. This procedure yields the $\beta$-intensity distribution related to $\beta$p emission, displayed in fig. 9. This spectrum, which takes the proton-separation energy of $2210 \pm 40$ keV in $^{103}$In [38] into account, was used for determining the proton branching ratio of $1.2 \pm 0.1\%$ and for deducing the GT strength distribution related to the $\beta$p decay. The intensities of the $^{103}$Sn $\beta$p-decay to the ground and first excited states of $^{102}$Cd are shown in fig. 11 in comparison with the statistical model calculations, discussed in sect. 4.1. The branching ratios for corresponding $\beta^+$p and ECp transitions, deduced from these proton intensities, are shown in table 3.

For a selected $^{102}$Cd state, the slope of the ratio of the ECp and $\beta^+$p intensities ($I_{\mathrm{ECp}}/I_{\beta^+\mathrm{p}}$) as a function of the proton energy depends only on the energy window open for these two decay modes, and can thus be used to determine the $Q_{\mathrm{EC}} - S_{\mathrm{p}}$ value. The corresponding results for the decay of $^{103}$Sn to the $^{102}$Cd ground state are shown in fig. 12. The experimental data were fitted by using the theoretical ratio of the statistical rate functions for $\beta^+$

emission and EC decay [39]. The $Q_{\rm EC} - S_{\rm p}$ value was the only free parameter in this fit. The resulting $Q_{\rm EC} - S_{\rm p}$ value is $5400 \pm 100$ keV. The major part of the uncertainty is due to the inaccuracy of the proton energy calibration. This $Q_{\rm EC} - S_{\rm p}$ value, together with the known $^{103}$In proton-separation energy of $2210 \pm 40$ keV [38], yields a $Q_{\rm EC}$ value of $7610 \pm 110$ keV for the $^{103}$Sn decay. This $Q_{\rm EC}$ value agrees with the one determined in sect. 3.2.2 from the EC/$\beta^+$ ratio. The weighted average for $Q_{\rm EC}$ is $7640 \pm 70$ keV, compared to a value of $7630 \pm 300$ keV extrapolated from systematic trends [38].

### 3.3 $1/2^-$ isomer in $^{103}$In

The presence of a long-lived $1/2^-$ isomer in $^{103}$In with an excitation energy of 632 keV and a half-life of $34 \pm 2$ s has been reported in refs. [40] and [26]. In the measurement with the Si-Ge array we did not observe $\gamma$-rays depopulating the isomeric state because of the short time gate for $\beta$-$\gamma$ coincidences (see sect. 2.2). However, transitions from the $1/2^-$ isomeric level were registered in the TAS measurement. The NaI crystal of the TAS was used as an active shielding of the GeX and Si detectors. By demanding anticoincidence with NaI signals, the 632 keV $\gamma$-rays as well as the corresponding conversion electrons were detected by the GeX and Si detectors, respectively.

The $\beta$-decay and internal-transition (IT) branches of $^{103m}$In are known to be 67% and 33%, respectively [26]. By using the TAS, the intensity of the IT branch was measured to be about 8(2)% of all $^{103}$Sn decays. This value was obtained in a conversion-electron measurement, requiring events in the TOP and/or BOT detectors to be in anticoincidence with NaI signals. This gives a total intensity of about 24% of all $^{103}$Sn decays feeding the $1/2^-$ state. The unplaced $\gamma$-ray transitions of 643, 994, 1071, 1134, 1548, 1579, 1958 and 2049 keV (see table 1) are candidates to feed the isomeric state. The most intense of those being the 643 keV transition has an intensity of 6% per $^{103}$Sn decay. If one assumes that this line directly populates the isomer, a level at 1275 keV is established. The systematics of light odd-$A$ indium isotopes, displayed in fig. 13, shows the presence of low-lying $1/2^-$ isomers in the neighbouring $^{105}$In [41] and $^{107}$In [42] nuclei. In $^{105}$In the $1/2^-$ isomeric level is fed by two transitions with energies of 629 and 536 keV [43] and intensities similar to that of the 643 keV line (see also table 1). It is thus tentatively suggested to place the 643 keV transition as one feeding the $1/2^-$ isomeric state in $^{103}$In. However, there is no indication of any direct $\beta$ feeding of the 1275 keV level in the TAS data, while it may well be populated by $\gamma$ decay of higher-lying states.

The $(5/2^-)$ level in $^{107}$In lying at 840 keV above the $1/2^-$ isomer is shown in fig. 13. The 994 keV unplaced gamma ray in the $^{103}$Sn decay could be an analogue of $(5/2^-) \rightarrow 1/2^-$ transition in $^{107}$In, albeit no such a transition has been found in $^{105}$In. The analogous transition in $^{109}$In has an energy of 791 keV [44]. Another unplaced 780 keV transition, found in this work, cannot populate the isomeric state, since it was found to be in coincidence with the 351 keV transition from the other cascade.

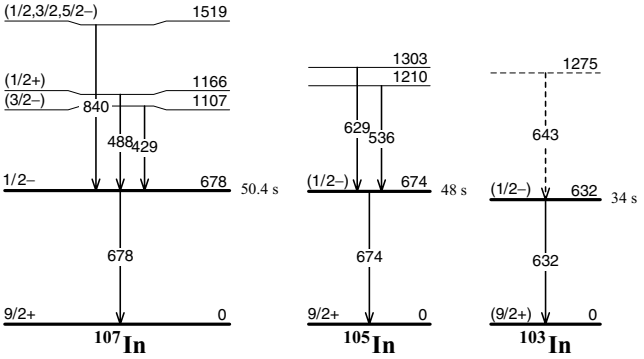


**Fig. 13.** Systematics of low-lying levels for light odd-$A$ indium isotopes. Only transitions feeding an isomer are shown. The data were taken from [41,42] for $^{107}$In, [40,43] for $^{105}$In and [26] for $^{103}$In.

## 4 Discussion

### 4.1 Beta-delayed proton decay of $^{103}$Sn

A statistical model calculation was performed in order to interpret the proton-intensity distribution. In this model the $5/2^+$ ground state of the $^{103}$Sn decays via allowed $\beta^+$/EC transitions to $I^\pi \in \{3/2^+; 5/2^+; 7/2^+\}$ states in $^{103}$In. The probability to populate such levels was assumed to be proportional to $(2I + 1)$. For the statistical model calculation the distribution of the experimental $\beta$ intensity, displayed in fig. 9, was used. For the level density of intermediate states in $^{103}$In the shell model prediction was employed (see sect. 4.2, *Model A*).

The $^{103}$In states populated in $\beta$ decay de-excite via $\gamma$-ray or proton emission. The corresponding radiative widths were calculated by using the statistical model of nuclear electromagnetic de-excitation [45]. The proton widths for the $^{103}$In levels that decay into the $^{102}$Cd ground and first excited states were obtained as described in ref. [46]. The coefficients for the proton-barrier transmission were calculated by using a set of optical-model potential parameters from ref. [47].

In order to reproduce within the statistical model calculation the experimental value of $1.2 \pm 0.1$% for the proton branching ratio (see sect. 3.2.3), the $\gamma$ widths of the relevant $^{103}$In states were reduced by 30%. The resulting shape of the proton-intensity distributions is in good agreement with the experimental data (see fig. 11). This model also reproduces the experimental branching ratio of $\beta$p transitions to the ground and first excited states of $^{102}$Cd. The shift of about 150 keV of the mean proton energy between calculation and experiment probably indicates that the model calculation is based on an incorrect energy dependence of the $\gamma$ widths of the $^{103}$In states.

The measurement of $K$ X-rays in coincidence with the $\beta$p decay of $^{103}$Sn, shown in the lower panel of fig. 4, allowed us to deduce the intensity ratio $I_K(\mathrm{In})/I_K(\mathrm{Cd})$. The resulting upper limit of $4 \pm 2$% is in agreement with the value of 2% obtained in the statistical model calculation described above. Using this ratio and the total width of the $K$-shell vacancy state in a tin atom of 8.53 eV [48],

the mean width of excited nuclear states in $^{103}$In was determined to be $0.3 \pm 0.2$ eV (for more details about this method see [49,50]).

### 4.2 $^{103}$In level scheme

The shell-model calculations were performed by means of the code OXBASH [51] in the $\pi(1g_{9/2},\, 2p_{1/2})^{11}$– $\nu(1g_{7/2},\, 2d_{5/2},\, 2d_{3/2},\, 3s_{1/2},\, 1h_{11/2})^4$ model space, using realistic effective interaction [30] and considering $^{88}$Sr as an inert core. The single particle energies were chosen to reproduce the single proton hole and single neutron particle energies in $^{100}$Sn [31]. This model approach will be denoted *Model A* further on. As an alternative approach we will discuss in sect. 4.4 results from a shell model calculation in the same model space using an empirical interaction as described in refs. [28,52], which will be denoted as *Model B* in the further discussion. The shell-model structure of positive-parity levels in $^{103}$In is governed by the coupling of a $\pi(1g_{9/2})$ hole to the four neutrons above the $N = 50$ closed shell. The ground state of $^{103}$In is assumed to be $I^\pi = 9/2^+$ [19]. In fig. 3 the experimental level scheme obtained in the present work is compared to the shell-model results of *Model A*. The coupling of the $\pi(1g_{9/2})$ state to the $I^\pi{=}2^+$ state in $^{104}$Sn gives rise to the multiplet $I^\pi{=}(5/2^+,\, 7/2^+,\, 9/2^+,\, 11/2^+,\, 13/2^+)$. This set of states is separated by an energy gap of about 300 keV from the other higher-lying levels in the shell-model predictions as well as in the experimental level scheme (see fig. 3). Two lower-lying levels of the multiplet, at the energies of 1078 and 1273 keV, are known to have $11/2^+$ and $13/2^+$ assignment [19], respectively. For the 1429 keV level the spin-parity of $(9/2^+)$ was suggested (see. 3.1). The levels at 1356 and 1397 energy are expected to be $5/2^+$ and $7/2^+$ states. In the shell-model calculation this multiplet is shifted upwards by about 300 keV, which is due to a too strong pairing in the $^{104}$Sn ground state. A correction would require a tuning of the realistic interaction which is outside the scope of the present paper.

The $1/2^-$ state is predicted by the shell-model calculation with the original two-body matrix elements (TBME) to be at an energy of 1372 keV. This is about 700 keV higher than the experimentally measured value of 632 keV (see sect. 3.3). The discrepancy is due to the untuned $\pi p_{1/2}\nu(d_{5/2}, g_{7/2})$ monopole interaction. A monopole shift of 250 keV to $\pi p_{1/2}\nu d_{5/2}$ multiplet and 200 keV to the $\pi p_{1/2}\nu g_{7/2}$ multiplet brings the $1/2^-$ state to 664 keV (see fig. 3). As a side effect this correction reproduces the $Z = 40$ shell gap in $^{96}$Zr, which is predicted too high with the original TBME, and is determined by the same monopoles.

### 4.3 Ground-state spin and parity assignment of $^{103}$Sn

The $5/2^+$ assignment for the $^{103}$Sn ground state is based on a systematical comparison with the other odd-A neutron-deficient tin isotopes [3]. If one assumes, in contrast to this assignment, the $\nu g_{7/2}$ shell-model state to form the ground state of $^{103}$In, the above-mentioned shell model calculation predicts a $\beta$ intensity of 6% for its GT decay to the $^{103}$In ground state. This prediction, compared to the upper limit of 1% for the ground-state–to–ground-state $\beta$ intensity (see sect. 3.2.2) yields further evidence for assigning $5/2^+$ to the ground state of $^{103}$Sn.

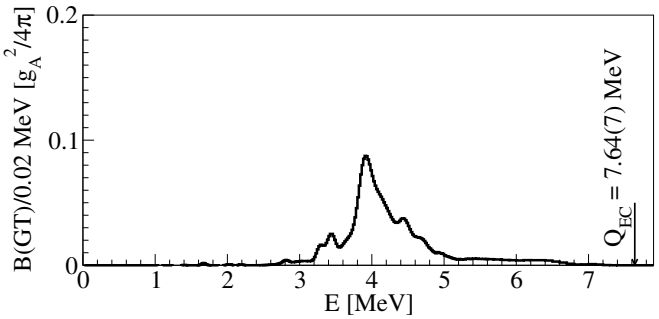


**Fig. 14.** GT strength distribution for $^{103}$Sn obtained from the TAS measurement (black-line histogram) and resulting from shell-model calculations: *Model A* (grey-line histogram) and *Model B* (dotted histogram), introduced in sects. 4.2. The theoretical distributions were normalized to the summed experimental $B$(GT) value (see text).

### 4.4 Gamow-Teller strength distribution of $^{103}$Sn

For an allowed GT transition, the GT strength ($B$(GT)) in units of $g_A^2/4\pi$ can be calculated according to

$$B(\mathrm{GT}) = \frac{D \cdot I_\beta(E)}{f(Q_{\mathrm{EC}} - E) \cdot T_{1/2}},$$

where $D = 3860 \pm 18$ s denotes the constant corresponding to the value of $g_A$ for the decay of the free neutron [53, 54], and $I_\beta$ the normalized $\beta$ intensity, $E$ the excitation energy of the daughter nucleus, and $f$ the statistical rate function.

The GT strength, displayed in fig. 14, was calculated using the $Q_{\mathrm{EC}}$ value of $7660 \pm 100$ keV, obtained from the deconvolution procedure (see sect. 3.2.2), the half-life of $7.0 \pm 0.2$ s (see table 2), and the $I_\beta$ distribution shown in fig. 9. The summed GT strength $\sum B(\mathrm{GT})$ of $^{103}$Sn was obtained as $3.5 \pm 0.5$, with fractions of $0.42 \pm 0.06$ and $3.1 \pm 0.5$ being related to $\beta$p and $\beta$-delayed $\gamma$-ray emission, respectively.

The resonance-like shape of the experimental GT strength distribution, shown in fig. 14, peaks at an $^{103}$In excitation-energy of about 3.9 MeV. These decay characteristics are interpreted as the $\pi g_{9/2} \rightarrow \nu g_{7/2}$ GT transformation occurring within the even-even core and leading to three-quasiparticle states in the odd-$Z$, even-$N$ daughter nucleus. Figure 14 shows also the theoretical $B$(GT) distributions obtained from shell-model calculations, namely *Model A* and *Model B*. Both theoretical curves were normalized to the summed experimental GT strength, as the shell model predicts the $\sum B(\mathrm{GT})$ value to be significantly larger than the measured one. This "quenching"

or "hindrance" can be expressed as a ratio of the shell-model $\sum B(\mathrm{GT})$ value to the experimental one. For $^{103}$Sn a quenching value of $4.3 \pm 0.6$ was obtained. Most of the hindrance is believed to be explained by core polarization and higher-order configuration mixing [55]. *Model A* predicts the position of the GT resonance about 500 keV too high, while the width and the high-energy strength are slightly overpredicted. *Model B* misses the resonance by about 300 keV to the low-energy side which could be due to the reversed $2d_{5/2}$ - $1g_{7/2}$ level order obtained in this model for $^{101}$Sn, *i.e.* the $\pi g_{9/2}\nu(d_{5/2}, g_{7/2})$ monopole interaction. It has been shown that the underpredicted width of the resonance can be increased by a renormalisation of the $\pi g_{9/2}\nu g_{7/2}$ interaction [17].

## 5 Summary

The development of $SnS^+$ beams at the GSI on-line mass separator allowed us to study the $\beta$-decay properties of the very neutron-deficient isotope $^{103}$Sn and thereby gain information about the GT $\beta$-decay in the region of the doubly-magic nucleus $^{100}$Sn. By using the Si-Ge array, 31 (29 new) $\beta$-delayed $\gamma$-rays of the $^{103}$Sn decay were identified; 20 of them were placed in the decay scheme of $^{103}$Sn, constructed on the basis of the $\gamma$-$\gamma$ coincidence analysis. The TAS data show that the GT strength distribution of $^{103}$Sn is characterized by a dominant resonance occurring at $^{103}$In excitation energies of about 3.9 MeV. This observation is compatible with the simple picture according to which this decay occurs withing the even-even core leading to three-quasi-particle states which correspond to the $\pi(g_{9/2})^{-1}\nu(d_{5/2}, g_{7/2})^4$ shell-model configuration. The model predicts the total GT strength 4.3 times higher than the experimental $\sum B(\mathrm{GT})$ value. Our experiment has yielded for the first time information on the proton-branching ratio ($1.2 \pm 0.1\%$), $Q_{\mathrm{EC}}$ value ($7.64 \pm 0.7$ MeV) and the EC/total ratio ($0.20 \pm 0.02$) of the $^{103}$Sn decay. All in all, these data indicate the dominant role of the even-even core decay, in particular for the large $Q_{\mathrm{EC}}$ windows of light tin isotopes. They also represent a considerable improvement of the experimental know-how required for further progress in decay studies near $^{100}$Sn.

The authors would like to thank K. Burkard and W. Hüller for their contribution to the development and operation of the GSI on-line mass separator. Authors from Warsaw acknowledge support from the Polish Committee of Scientific Research under KBN Grant 2 P03B 035 23.

## References

1. R. Schneider *et al.*, Z. Phys. A **348**, 241 (1994).
2. M. Lewitowicz *et al.*, Phys. Lett. B **332**, 20 (1994).
3. C. Fahlander *et al.*, Phys. Rev. C **63**, 021307 (2001).
4. M. Lipoglavšek *et al.*, Phys. Rev. C **66**, 011302 (2002).
5. M. Lipoglavšek *et al.*, Phys. Rev. Lett. **76**, 888 (1996).
6. M. Górska *et al.*, Phys. Rev. Lett. **79**, 2415 (1997).
7. A. Blazhev *et al.*, Phys. Rev. C **69**, 064304 (2004).
8. R.J. Tighe *et al.*, Phys. Rev. C **49**, R2871 (1994).
9. Z. Liu *et al.*, *Re-investigation of direct proton decay of $^{105}Sb$*, GSI Scientific Report 2004, GSI 2005-1, p. 85 and to be published.
10. Z. Janas *et al.*, Phys. Scr. **T56**, 262 (1995).
11. M. Karny *et al.*, Eur. Phys. J. A **25**, s01, 135 (2005), DOI: 10.1140/epjad/i2005-06-037-9.
12. C. Plettner *et al.*, Phys. Rev. C **66**, 044319 (2002).
13. M. Gierlik *et al.*, Nucl. Phys. A **724**, 313 (2003).
14. C. Plettner *et al.*, Nucl. Phys. A **733**, 20 (2004).
15. S. Harissopulos *et al.*, *Beta decay $^{95}Ag$*, to be published.
16. L. Batist *et al.*, Nucl. Phys. A **720**, 245 (2003).
17. Z. Hu *et al.*, Phys. Rev. C **60**, 024315 (1999).
18. Z. Hu *et al.*, Phys. Rev. C **62**, 064315 (2000).
19. J. Kownacki *et al.*, Nucl. Phys. A **627**, 239 (1997).
20. R. Kirchner, Nucl. Instrum. Methods Phys. Res. B **204**, 179 (2003).
21. I. Mukha *et al.*, Phys. Rev. C **70**, 044311 (2004).
22. J. Eberth *et al.*, Nucl. Instrum. Methods Phys. Res. A **369**, 135 (1996).
23. J. Gerl *et al.*, *Proceedings of the Conference on Physics from Large $\gamma$ ray Detector Arrays, Berkeley, USA, 1994* (LBL 35687, UC 413, 1994) p. 159.
24. A. Gadea *et al.*, Phys. Lett. B **619**, 88 (2005).
25. M. Karny *et al.*, Nucl. Instrum. Methods Phys. Res. B **126**, 411 (1997).
26. J. Szerypo *et al.*, Z. Phys. A **359**, 117 (1997).
27. P. Tidemand-Petersson *et al.*, Z. Phys. A **302**, 343 (1981).
28. K. Rykaczewski, GSI-95-09 (1995).
29. A. Stolz, PhD Thesis, TU München (2001).
30. M. Hjorth-Jensen, T.T.S. Kuo, E. Osnes, Phys. Rep. **261**, 125 (1995).
31. H. Grawe, M. Lewitowicz, Nucl. Phys. A **693**, 116 (2001).
32. M. Karny *et al.*, Nucl. Phys. A **640**, 3 (1998).
33. S. Agostinelli *et al.*, Nucl. Instrum. Methods Phys. Res. A **506**, 250 (2003).
34. J.C. Hardy, Phys. Lett. B **109**, 242 (1982).
35. J. Kopecky, M. Uhl, Phys. Rev. C **41**, 1941 (1990).
36. J. Speth, A. van der Woude, Rep. Prog. Phys. **44**, 719 (1981).
37. W.V. Prestwich *et al.*, Z. Phys. A **315**, 103 (1984).
38. G. Audi *et al.*, Nucl. Phys. A **729**, 3 (2003).
39. N.B. Gove, M.J. Martin, Nucl. Data Tables A **10**, 205 (1971).
40. P. Decrock, Lincentiaats Thesis, Leuven University (1988).
41. D. De Frenne, J. Jacobs, Nucl. Data Sheets **68**, 935 (1993).
42. J. Blachot, Nucl. Data Sheets **89**, 213 (2000).
43. M. Pfützner *et al.*, Nucl. Phys. A **581**, 205 (1995).
44. J. Blachot, Nucl. Data Sheets **86**, 505 (1999).
45. A. Cameron, Can. J. Phys. **35**, 666 (1956).
46. P. Hornshøj *et al.*, Nucl. Phys. A **187**, 609 (1972).
47. C.H. Johnson *et al.*, Phys. Rev. C **20**, 2052 (1979).
48. J.L. Campbell, Tibor Papp, At. Data Nucl. Data Tables **77**, 1 (2001).
49. J.C. Hardy *et al.*, Phys Rev. Lett. **37**, 133 (1976).
50. Z. Janas *et al.*, Eur. Phys. J. A **23**, 197 (2005).
51. B.A. Brown, A. Etchegoyen, W.D.M. Rae, computer code OXBASH, MSU-NSCL report No. 524 (1988).
52. B.A. Brown, K. Rykaczewski, Phys. Rev. C **50**, R2270 (1994).
53. E. Klempt *et al.*, Z. Phys. C **37**, 179 (1988).
54. S.J. Freedman, Comments Nucl. Part. Phys. **19**, 209 (1990).
55. I.S. Towner, Nucl. Phys. A **444**, 402 (1985).